Smart Mater. Struct. **22** (2013) 015002 (14pp) doi:10.1088/0964-1726/22/1/015002

Electroelastic modeling and experimental validations of piezoelectric energy harvesting from broadband random vibrations of cantilevered bimorphs

S Zhao and A Erturk

G W Woodruff School of Mechanical Engineering, Georgia Institute of Technology, Atlanta, GA 30332, USA

E-mail: alper.erturk@me.gatech.edu

Received 21 August 2012, in final form 8 October 2012
Published 30 November 2012
Online at stacks.iop.org/SMS/22/015002

Abstract
We present electroelastic modeling, analytical and numerical solutions, and experimental validations of piezoelectric energy harvesting from broadband random vibrations. The modeling approach employed herein is based on a distributed-parameter electroelastic formulation to ensure that the effects of higher vibration modes are included, since broadband random vibrations, such as Gaussian white noise, might excite higher vibration modes. The goal is to predict the expected value of the power output and the mean-square shunted vibration response in terms of the given power spectral density (PSD) or time history of the random vibrational input. The analytical method is based on the PSD of random base excitation and distributed-parameter frequency response functions of the coupled voltage output and shunted vibration response. The first of the two numerical solution methods employs the Fourier series representation of the base acceleration history in an ordinary differential equation solver while the second method uses an Euler–Maruyama scheme to directly solve the resulting electroelastic stochastic differential equations. The analytical and numerical simulations are compared with several experiments for a brass-reinforced PZT-5H bimorph under different random excitation levels. The simulations exhibit very good agreement with the experimental measurements for a range of resistive electrical boundary conditions and input PSD levels. It is also shown that lightly damped higher vibration modes can alter the expected power curve under broadband random excitation. Therefore, the distributed-parameter modeling and solutions presented herein can be used as a more accurate alternative to the existing single-degree-of-freedom solutions for broadband random vibration energy harvesting.

1. Introduction

Vibration-based energy harvesting for low-power electricity generation has been heavily researched over the past decade [1–5]. The motivation in this research field is due to the reduced power requirement of small electronic components, such as the wireless sensor networks used in passive and active monitoring applications. The goal is to eliminate the need for battery replacement and disposal by enabling autonomous wireless electronic systems. Among the basic transduction mechanisms that can be used for vibration-to-electricity conversion (electromagnetic, electrostatic, piezoelectric, and magnetostrictive conversion methods as well as the use of electroactive polymers [6–16]), piezoelectric transduction has received the greatest attention due to the high-power density and ease of application of piezoelectric materials [4].

Most of the existing electromechanical modeling efforts on vibration-based energy harvesting have been based on

the assumption that the vibrational input is deterministic, as in the typical case of harmonic excitation of linear and nonlinear energy harvesters at or around resonance [6–16]. Closed-form expressions for the optimal conditions have been developed by several authors for deterministic forms of excitation [17–20]. These efforts contribute to the design and performance evaluation of linear and nonlinear energy harvesters under harmonic excitation.

Harmonic excitation is a simple and rather idealized representation of real-world ambient vibrations. In many cases, ambient vibrational energy is non-harmonic or entirely stochastic, with broad frequency content. As compared to the literature of harvesting deterministic forms of energy, rather few research groups have investigated energy harvesting from random vibrations and employed different electromechanical models. Typically, the excitation source is assumed to be ideal white noise, which is a broadband random signal that has a flat power spectral density (PSD) in the frequency domain.

Single-degree-of-freedom (SDOF) modeling is the most commonly used approach in the theoretical exploration of energy harvesters driven by broadband random excitation. Halvorsen [21] derived closed-form expressions for the power output, optimal load, and proof mass displacement based on linear SDOF modeling, and verified the resulting expressions by solving the Fokker–Planck equation. The results were also compared with those obtained from the same model under harmonic excitation and differences were reported. Adhikari *et al* [22] also used a linear SDOF model to describe the stochastic dynamics for the fundamental vibration mode of an energy harvester. Analytical expressions of the harvested power and optimal load were derived, and illustrated using numerical examples. Scruggs [23] investigated the optimal control of a linear energy harvester network for increased power flow to a storage system under random excitation.

Daqaq [24] considered hardening stiffness in the SDOF formulation for electromagnetic energy harvesting and concluded that the monostable Duffing oscillator did not provide an enhancement over the typical linear oscillators under Gaussian white and colored random excitations, and contemporaneous experiments by Barton *et al* [25] for electromagnetic energy harvesting provided consistent results. Based on SDOF modeling, Gammaitoni *et al* [26] suggested that carefully designed nonlinear oscillators could potentially outperform the linear ones under noise excitation for both bistable and monostable configurations.

Ferrari *et al* [27] numerically studied a bistable SDOF energy harvesting system under broadband random excitation using the Euler–Maruyama method. Litak *et al* [28] numerically simulated a bistable piezomagnetoelastic energy harvester (introduced by Erturk *et al* [29]) under Gaussian white noise and observed a positive correlation between standard deviations of the random excitation and of the voltage output. In particular, they [28] focused on the potential of exploiting 'stochastic resonance' in energy harvesting, as formerly discussed by McInnes *et al* [30] through another SDOF representation. Ali *et al* [31] developed a linearized SDOF model for broadband random excitation of bistable piezomagnetoelastic energy harvesters. They showed that there existed a cut-off standard deviation of the input excitation below which the power output was very low. Daqaq [32] gave a theoretical study on the response of an inductive SDOF bistable energy harvester to white and exponentially correlated Gaussian noise. For Gaussian white noise excitation, the exact probability distribution function was expressed in order to obtain a closed-form expression of mean power output.

Nguyen *et al* [33] studied a wideband MEMS electrostatic energy harvester using a lumped-parameter model. They experimentally compared the PSD of voltage output for different levels of broadband random inputs. They also examined the relationship between the output power and PSD of excitation in addition to providing finite-element simulations. Some research groups also utilized SPICE, a numerical circuit simulator, to simulate the harvested energy in response to random vibrations [34–36]. Tvedt *et al* [37] also considered broadband vibration excitation when they investigated the nonlinear behavior of an electrostatic energy harvester, along with the effect of bias voltage.

As an alternative to the aforementioned SDOF modeling and analysis efforts, in this paper, distributed-parameter electroelastic modeling, analytical and numerical solutions, and experimental validations of piezoelectric energy harvesting from broadband random vibrations are presented. The motivation for distributed-parameter modeling emerges from the fact that broadband random vibrations can in fact excite higher vibration modes of an electroelastic energy harvester, which can be significant for a configuration with lightly damped higher modes. In the following sections, first the distributed-parameter electroelastic model employed in the analytical and numerical simulations is summarized. Then the expected power and mean-square shunted vibration response are expressed in terms of the base acceleration PSD and the electroelastic frequency response functions (FRFs) in the analytical solution. After that, the numerical electroelastic solutions are presented based on two separate approaches. The deterministic approach represents the base acceleration history in terms of its Fourier series expansion to use in the first-order electroelastic equations, while the stochastic approach directly employs an Euler–Maruyama scheme to solve the resulting first-order stochastic differential equations. Experimental results are then presented to validate analytical and numerical predictions. Electrical power generation and its shunt damping effect at different random vibration levels are investigated.

2. Governing electroelastic equations and harmonic excitation

2.1. Distributed-parameter electroelastic modeling

Figure 1 shows symmetric bimorph piezoelectric energy harvester configurations excited by base motion in the form of a translational displacement, $g(t)$, with a superimposed small rotational displacement, $h(t)$. The wires originating from negligibly thin and perfectly conductive electrode pairs covering the surfaces of the piezoceramic layers are connected

to a resistive electrical load (R_l). The distributed-parameter electroelastic formulation summarized in this section is based on the Euler–Bernoulli beam assumptions [11, 38]. Therefore, the energy harvesters considered herein are assumed to be thin structures so that the shear distortion and rotary inertia effects are negligible (we note that [38, 39] present modeling of piezoelectric energy harvesters with moderate thickness). As a consequence, the tensorial form of the linear piezoelectric constitutive equations can be given in the plane-stress form as

$$\begin{Bmatrix} T_1 \\ D_3 \end{Bmatrix} = \begin{bmatrix} \bar{c}_{11}^E & -\bar{e}_{31} \\ \bar{e}_{31} & \bar{\varepsilon}_{33}^S \end{bmatrix} \begin{Bmatrix} S_1 \\ E_3 \end{Bmatrix} \tag{1}$$

where T_1 is the stress component, D_3 is the electric displacement component, S_1 is the strain component, E_3 is the electric field component, the 3-direction is the poling direction (z-direction in figure 1), and the 1-direction is the axial direction (x-direction in figure 1). In addition, $\bar{e}_{31}$ is the effective piezoelectric stress constant, $\bar{c}_{11}^E$ is elastic stiffness component (Young's modulus) at constant electric field, and $\bar{\varepsilon}_{33}^S$ is the permittivity component at constant strain; an over-bar denotes that the respective parameter is reduced for the plane-stress conditions. Thus, for a beam-like thin cantilever, the plane-stress elastic, piezoelectric and dielectric parameters can be given in terms of the 3-D electroelasticity components as

$$\begin{gathered} \bar{c}_{11}^E = 1/s_{11}^E, \qquad \bar{e}_{31} = d_{31}/s_{11}^E, \\ \bar{\varepsilon}_{33}^S = \varepsilon_{33}^T - d_{31}^2/s_{11}^E \end{gathered} \tag{2}$$

where s_{11}^E is the elastic compliance at constant electric field, d_{31} is the commonly referred piezoelectric strain constant, and ε_{33}^T is the permittivity component at constant stress. Note that the substructure material is typically an isotropic metal.

The governing linear electroelastic equations of a bimorph piezoelectric energy harvester (figure 1) in the physical coordinates are [11, 38]

$$\begin{aligned} &D\frac{\partial^4 w_{\mathrm{rel}}(x,t)}{\partial x^4} + c_{\mathrm{s}}\frac{\partial^5 w_{\mathrm{rel}}(x,t)}{\partial x^4 \partial t} + c_{\mathrm{m}}\frac{\partial w_{\mathrm{rel}}(x,t)}{\partial t} \\ &\quad + m\frac{\partial^2 w_{\mathrm{rel}}(x,t)}{\partial t^2} - \vartheta v(t)\left[\frac{\mathrm{d}\delta(x)}{\mathrm{d}x} - \frac{\mathrm{d}\delta(x-L)}{\mathrm{d}x}\right] \\ &= -[m + M_t\delta(x-L)]\frac{\partial^2 w_{\mathrm{b}}(x,t)}{\partial t^2} \end{aligned} \tag{3}$$

$$C_{\mathrm{p}}^{\mathrm{eq}}\frac{\mathrm{d}v(t)}{\mathrm{d}t} + \frac{v(t)}{R_{\mathrm{l}}} + \vartheta\int_0^{\mathrm{L}}\frac{\partial^3 w_{\mathrm{rel}}(x,t)}{\partial x^2 \partial t}\mathrm{d}x = 0 \tag{4}$$

where $w_{\mathrm{b}}(x,t) = g(t) + xh(t)$ is the effective base displacement as the excitation input, $w_{\mathrm{rel}}(x,t)$ is the vibration response (transverse displacement of the neutral axis relative to the moving base at position x and time t), $v(t)$ is the voltage response across the external resistive load, D is the bending stiffness of the beam, m is the mass per unit length of the beam, c_{m} is the external damping coefficient (mass-proportional damping), c_{s} is the internal damping coefficient of the composite structure (stiffness-proportional damping), M_t is the tip mass, $C_{\mathrm{p}}^{\mathrm{eq}}$ is the equivalent capacitance of the piezoceramic layers, ϑ is the electromechanical coupling term in the physical coordinates, and $\delta(x)$ is the Dirac delta function. The electromechanical coupling term is $\vartheta = \bar{e}_{31}b(h_{\mathrm{p}} + h_{\mathrm{s}})/2$ if the piezoelectric layers are connected in series and $\vartheta = \bar{e}_{31}b(h_{\mathrm{p}} + h_{\mathrm{s}})$ if the piezoelectric layers are connected in parallel (where b is the width of the layers, h_{p} is the thickness of each piezoceramic layer, and h_{s} is the thickness of the substructure layer). Likewise the equivalent capacitance is $C_{\mathrm{p}}^{\mathrm{eq}} = \bar{\varepsilon}_{33}^S bL/2h_{\mathrm{p}}$ for series connection and $C_{\mathrm{p}}^{\mathrm{eq}} = 2\bar{\varepsilon}_{33}^S bL/h_{\mathrm{p}}$ for parallel connection (where L is the overhang length).

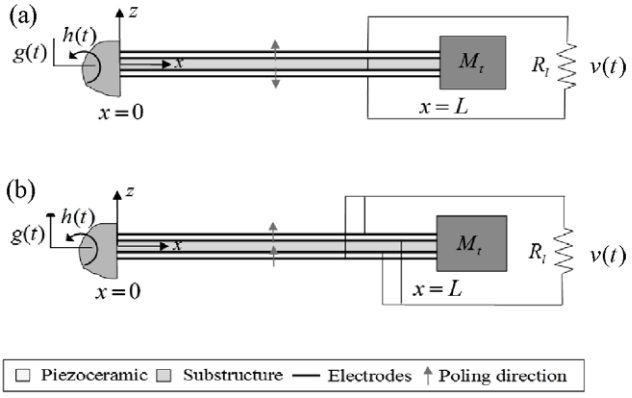

Figure 1. Bimorph piezoelectric energy harvester configurations under base excitation: (a) series and (b) parallel connection of the piezoelectric layers.

If the vibration response (relative to its moving base) in the physical coordinates is expressed in terms of the mass-normalized eigenfunctions (mode shapes), $\phi_r(x)$, and the modal coordinates, $\eta_r(t)$, for the rth mode such that

$$w_{\mathrm{rel}}(x,t) = \sum_{r=1}^{\infty}\phi_r(x)\eta_r(t) \tag{5}$$

where the eigenfunctions are obtained from the undamped and electromechanically uncoupled problem [11, 38], then, following the analytical modal analysis procedure [40], the electromechanically coupled ordinary differential equations in the modal coordinates are obtained as

$$\ddot{\eta}_r(t) + 2\zeta_r\omega_r\dot{\eta}_r(t) + \omega_r^2\eta_r(t) - \tilde{\theta}_r v(t) = f_r(t) \tag{6}$$

$$C_{\mathrm{p}}^{\mathrm{eq}}\dot{v}(t) + \frac{v(t)}{R_{\mathrm{l}}} + \sum_{r=1}^{\infty}\tilde{\theta}_r\dot{\eta}_r(t) = 0. \tag{7}$$

Here, an over-dot ($\dot{}$) represents differentiation with respect to time, ζ_r is the modal mechanical damping ratio, ω_r is the undamped natural frequency (close to the short-circuit resonance frequency, ω_r^{sc}, for the light mechanical damping condition: $\zeta_r \ll 1$), $\tilde{\theta}_r$ is the modal electromechanical coupling term, and $f_r(t)$ is the modal mechanical forcing function, which depends on the forms of $g(t)$ and $h(t)$.

2.2. Steady-state response to harmonic excitation

If the motion of the vibrating base in figure 1 is harmonic of the form $g(t) = W_0 e^{j\omega t}$ and $h(t) = \theta_0 e^{j\omega t}$ (where W_0 and θ_0 are the translational and small rotational displacement amplitudes

Table 1. Modal electromechanical coupling and equivalent capacitance terms for the (a) series and (b) parallel connection cases.

(a) Series connection	
$\tilde{\theta}_r$	$\bar{e}_{31}(h_p + h_s)b\phi_r'(L)/2$
C_p^{eq}	$\bar{\varepsilon}_{33}^S bL/2h_p$
(b) Parallel connection	
$\tilde{\theta}_r$	$\bar{e}_{31}(h_p + h_s)b\phi_r'(L)$
C_p^{eq}	$2\bar{\varepsilon}_{33}^S bL/h_p$

of the base, respectively, ω is the excitation frequency, and j is the unit imaginary number), hence $f_r(t) = F_r e^{j\omega t}$, the steady-state voltage response ($v(t) = Ve^{j\omega t}$, where V is the complex voltage) of the cantilevers shown in figure 1 can be given as [11, 38]

$$v(t) = Ve^{j\omega t} = \frac{\sum_{r=1}^{\infty} \frac{-j\omega\tilde{\theta}_r F_r e^{j\omega t}}{\omega_r^2 - \omega^2 + j2\zeta_r\omega_r\omega}}{\frac{1}{R_l} + j\omega C_p^{eq} + \sum_{r=1}^{\infty} \frac{j\omega\tilde{\theta}_r^2}{\omega_r^2 - \omega^2 + j2\zeta_r\omega_r\omega}}. \quad (8)$$

Here, the modal electromechanical coupling ($\tilde{\theta}_r$) and the equivalent inherent capacitance (C_p^{eq}) terms for the series and parallel connections of the piezoceramic layers are given in table 1 (where $\phi_r'(x)$ is the derivative of $\phi_r(x)$ with respect to x).

In equation (8), the modal mechanical forcing term due to base excitation is

$$F_r = \omega^2 W_0 \left(m \int_0^L \phi_r(x)\,dx + M_t\phi_r(L) \right) + \omega^2\theta_0 \left(\int_0^L x\phi_r(x)\,dx + M_t L\phi_r(L) \right). \quad (9)$$

The electromechanically coupled vibration response of the energy harvester beam (relative to its moving base) at steady state is then

$$w_{rel}(x,t) = \sum_{r=1}^{\infty} \frac{[f_r(t) + \tilde{\theta}_r v(t)]\phi_r(x)}{\omega_r^2 - \omega^2 + j2\zeta_r\omega_r\omega} = \sum_{r=1}^{\infty} \frac{[F_r + \tilde{\theta}_r V]\phi_r(x)e^{j\omega t}}{\omega_r^2 - \omega^2 + j2\zeta_r\omega_r\omega} \quad (10)$$

which includes the effect of piezoelectric shunt damping due to the $\tilde{\theta}_r v(t)$ term, where $v(t)$ is given by equation (8). Using equations (8) and (10), it is possible to define electroelastic FRFs.

2.3. Electroelastic FRFs: voltage output and shunted vibration response

If the base is assumed to be not rotating ($h(t) = 0$), i.e. $\theta_0 = 0$ in equation (9), but translating with $g(t) = W_0 e^{j\omega t}$, the modal mechanical forcing function becomes

$$F_r = -\sigma_r\omega^2 W_0 = \sigma_r A_0 \quad (11)$$

where A_0 is the base acceleration amplitude and σ_r is a modal forcing parameter:

$$\sigma_r = -m\int_0^L \phi_r(x)\,dx - M_t\phi_r(L). \quad (12)$$

One can then define the multi-mode voltage output-to-base acceleration FRF and the vibration response-to-base acceleration FRF as follows:

$$\alpha(\omega) = \frac{v(t)}{A_0 e^{j\omega t}} = \frac{\sum_{r=1}^{\infty} \frac{-j\omega\tilde{\theta}_r\sigma_r}{\omega_r^2 - \omega^2 + j2\zeta_r\omega_r\omega}}{\frac{1}{R_l} + j\omega C_p^{eq} + \sum_{r=1}^{\infty} \frac{j\omega\tilde{\theta}_r^2}{\omega_r^2 - \omega^2 + j2\zeta_r\omega_r\omega}} \quad (13)$$

$$\beta(\omega,x) = \frac{w_{rel}(x,t)}{A_0 e^{j\omega t}} = \sum_{r=1}^{\infty} \frac{\left[\sigma_r + \tilde{\theta}_r\alpha(\omega)\right]\phi_r(x)}{\omega_r^2 - \omega^2 + j2\zeta_r\omega_r\omega}. \quad (14)$$

The foregoing exact analytical solutions are typically truncated (in the simulations) after taking a sufficient number of modes (M modes) to represent the system dynamics in a given frequency range such that

$$\alpha(\omega) \cong \frac{\sum_{r=1}^{M} \frac{-j\omega\tilde{\theta}_r\sigma_r}{\omega_r^2 - \omega^2 + j2\zeta_r\omega_r\omega}}{\frac{1}{R_l} + j\omega C_p^{eq} + \sum_{r=1}^{M} \frac{j\omega\tilde{\theta}_r^2}{\omega_r^2 - \omega^2 + j2\zeta_r\omega_r\omega}} \quad (15)$$

$$\beta(\omega,x) \cong \sum_{r=1}^{M} \frac{[\sigma_r + \tilde{\theta}_r\alpha(\omega)]\phi_r(x)}{\omega_r^2 - \omega^2 + j2\zeta_r\omega_r\omega}. \quad (16)$$

If the energy harvester beam is excited close to a natural frequency, i.e., $\omega \cong \omega_r$, the contribution of all vibration modes other than the rth mode can be ignored in the summation terms of equations (15) and (16) as an approximation. One can then establish the *single-mode* voltage output-to-base acceleration FRF and the vibration response-to-base acceleration FRF as follows:

$$\hat{\alpha}(\omega) = \frac{-j\omega R_l\tilde{\theta}_r\sigma_r}{(1 + j\omega R_l C_p^{eq})(\omega_r^2 - \omega^2 + j2\zeta_r\omega_r\omega) + j\omega R_l\tilde{\theta}_r^2} \quad (17)$$

$$\hat{\beta}(\omega,x) = \frac{(1 + j\omega R_l C_p^{eq})\sigma_r\phi_r(x)}{(1 + j\omega R_l C_p^{eq})(\omega_r^2 - \omega^2 + j2\zeta_r\omega_r\omega) + j\omega R_l\tilde{\theta}_r^2} \quad (18)$$

where a hat ($\hat{}$) denotes that the respective expression is reduced for a single vibration mode (mode r) only. It should be noted that the foregoing single-mode relations are valid for excitation frequencies in the vicinity of the respective natural frequency only ($\omega \approx \omega_r$). Typically, the fundamental vibration mode is of interest (hence $r = 1$) and the single-mode FRFs become

$$\hat{\alpha}(\omega) = \frac{-j\omega R_l\tilde{\theta}_1\sigma_1}{(1 + j\omega R_l C_p^{eq})(\omega_1^2 - \omega^2 + j2\zeta_1\omega_1\omega) + j\omega R_l\tilde{\theta}_1^2} \quad (19)$$

$$\hat{\beta}(\omega,x) = \frac{(1 + j\omega R_l C_p^{eq})\sigma_1\phi_1(x)}{(1 + j\omega R_l C_p^{eq})(\omega_1^2 - \omega^2 + j2\zeta_1\omega_1\omega) + j\omega R_l\tilde{\theta}_1^2}. \quad (20)$$

3. Broadband random excitation: analytical solution

3.1. Expected value of the electrical power output

We consider the base excitation to be Gaussian white noise-type random signal, which has a constant PSD of S_0. That is, the input PSD covers the entire frequency band with constant amplitude. Using this property of the excitation along with the electroelastic FRFs summarized in the previous section, the analytical solution for the expected (mean) power can be derived.

Recalling that the electrical power output is simply $v^2(t)/R_l$, the expected value of the power output is

$$E[P(t)] = \int_{-\infty}^{\infty} \frac{S_0}{R_l} |\alpha(\omega)|^2 \, \mathrm{d}\omega. \tag{21}$$

Therefore, the multi-mode analytical solution for the expected power output is obtained from

$$E[P(t)] = \int_{-\infty}^{\infty} \frac{S_0}{R_l} \left| \frac{\sum_{r=1}^{\infty} \frac{-\mathrm{j}\omega\tilde{\theta}_r\sigma_r}{\omega_r^2-\omega^2+\mathrm{j}2\zeta_r\omega_r\omega}}{\frac{1}{R_l}+\mathrm{j}\omega C_p^{eq}+\sum_{r=1}^{\infty}\frac{\mathrm{j}\omega\tilde{\theta}_r^2}{\omega_r^2-\omega^2+\mathrm{j}2\zeta_r\omega_r\omega}} \right|^2 \mathrm{d}\omega \tag{22}$$

which is the exact representation considering the entire spectrum of excitation and all vibration modes of the harvester.

For a compact and closed-form representation, the single-mode solution of the expected power (for the fundamental vibration mode) is estimated from

$$E[P(t)] \cong E[\hat{P}(t)] = \int_{-\infty}^{\infty} \frac{S_0}{R_l} |\hat{\alpha}(\omega)|^2 \, \mathrm{d}\omega. \tag{23}$$

Employing equation (19) in (23) yields

$$E[\hat{P}(t)] = \int_{-\infty}^{\infty} \frac{S_0}{R_l} \times \left| \frac{-\mathrm{j}\omega R_l\tilde{\theta}_1\sigma_1}{(1+\mathrm{j}\omega R_l C_p^{eq})(\omega_1^2-\omega^2+\mathrm{j}2\zeta_1\omega_1\omega)+\mathrm{j}\omega R_l\tilde{\theta}_1^2} \right|^2 \times \mathrm{d}\omega. \tag{24}$$

Using the integration tables [41], equation (24) can be reduced to

$$E[\hat{P}(t)] = \{\pi S_0 R_l\tilde{\theta}_1^2\sigma_1^2\}\{R_l\tilde{\theta}_1^2 + 2\zeta_1\omega_1[(1+R_l^2\tilde{\theta}_1^2C_p^{eq}) + (2\zeta_1+R_lC_p^{eq}\omega_1)(R_lC_p^{eq}\omega_1)]\}^{-1} \tag{25}$$

which is analogous to the SDOF derivations given by Halvorsen [12] and Adhikari *et al* [13]. Equation (25) excludes all vibration modes other than the fundamental mode in the calculation of the expected power. This single-mode approximation leads to a simple estimate for the optimal electrical load (R_l^*) for the maximum power output:

$$\frac{\partial}{\partial R_l}\{E[\hat{P}(t)]\}\bigg|_{R_l=R_l^*} = 0 \rightarrow R_l^* = \frac{1}{\sqrt{(C_p^{eq})^2\omega_1^2 + C_p^{eq}\tilde{\theta}_1^2}}. \tag{26}$$

Back substitution yields the following expression for the single-mode estimate of the optimal expected power output:

$$E[\hat{P}(t)]_{R_l=R_l^*} = \left\{\pi S_0\sigma_1^2\tilde{\theta}_1^2\sqrt{(C_p^{eq})^2\omega_1^2 + C_p^{eq}\tilde{\theta}_1^2}\right\} \left\{4C_p^{eq}\tilde{\theta}_1^2\omega_1\zeta_1 + 4(C_p^{eq})^2\omega_1^3\zeta_1 + (\tilde{\theta}_1^2 + 4C_p^{eq}\omega_1^2\zeta_1^2)\sqrt{(C_p^{eq})^2\omega_1^2 + C_p^{eq}\tilde{\theta}_1^2}\right\}^{-1}. \tag{27}$$

Note that, when computing analytical solutions (particularly the multi-mode solution) by performing the frequency-domain integration numerically, the frequency range is set to be $[-\bar{\omega}, \bar{\omega}]$ such that

$$E[P(t)] = \int_{-\bar{\omega}}^{\bar{\omega}} \frac{S_0}{R_l} |\alpha(\omega)|^2 \, \mathrm{d}\omega \tag{28}$$

where $\bar{\omega}$ is large enough to ensure the coverage of major vibration modes contributing to the power output given the input PSD.

3.2. Mean-square value of the shunted vibration response

The multi-mode solution for the mean-square value of the vibration response (in the displacement form) relative to moving base at point x is

$$E[w_{rel}^2(x,t)] = \int_{-\infty}^{\infty} S_0 |\beta(\omega,x)|^2 \, \mathrm{d}\omega \tag{29}$$

yielding

$$E[w_{rel}^2(x,t)] = \int_{-\infty}^{\infty} S_0 \left| \sum_{r=1}^{\infty} \frac{[\sigma_r + \tilde{\theta}_r\alpha(\omega)]\phi_r(x)}{\omega_r^2-\omega^2+\mathrm{j}2\zeta_r\omega_r\omega} \right|^2 \mathrm{d}\omega. \tag{30}$$

The single-mode approximation for the fundamental vibration mode is

$$E[w_{rel}^2(x,t)] \cong E[\hat{w}_{rel}^2(x,t)] = \int_{-\infty}^{\infty} S_0 |\hat{\beta}(\omega,x)|^2 \, \mathrm{d}\omega. \tag{31}$$

Using equation (20) in (31) yields

$$E[\hat{w}_{rel}^2(x,t)] = \{\pi S_0\sigma_1^2\phi_1^2(x)[(C_p^{eq})^2R_l^2\omega_1^2 + 2\zeta_1C_p^{eq}R_l\omega_1 + 1]\}\{\omega_1^2[2(C_p^{eq})^2R_l^2\omega_1^3\zeta_1 + 2C_p^{eq}R_l^2\tilde{\theta}_1^2\omega_1\zeta_1 + 4C_p^{eq}R_l\omega_1^2\zeta_1^2 + R_l\tilde{\theta}_1^2 + 2\zeta_1\omega_1]\}^{-1} \tag{32}$$

from which the optimal electrical load (R_l^{**}) of maximum shunt damping is obtained as

$$\frac{\partial}{\partial R_l}\{E[\hat{w}_{rel}^2(x,t)]\}\bigg|_{R_l=R_l^{**}} = 0 \rightarrow R_l^{**} = \frac{1}{\omega_1C_p^{eq}(1-2\zeta_1)}. \tag{33}$$

Back substitution leads to the minimum mean-square vibration response for the electrical load of the maximum shunt damping:

$$E[\hat{w}_{rel}^2(x,t)]_{R_l=R_l^{**}} = \frac{2\pi S_0C_p^{eq}\sigma_1^2(1-\zeta_1)\phi_1^2(x)}{\omega_1(\tilde{\theta}_1^2 - 4C_p^{eq}\omega_1^2\zeta_1^2 + 4C_p^{eq}\omega_1^2\zeta_1)}. \tag{34}$$

In the experiments, it is common practice to measure the velocity response (rather than displacement) of the cantilever relative to the fixed reference frame (rather than moving base). Therefore, it is useful to modify the theoretical vibration response to predict the velocity measurement rather than post-processing the experimental data. The multi-mode solution for the mean-square velocity response at the free end of the bimorph is given by

$$E[\dot{w}^2(L,t)] = \int_{-\infty}^{\infty} S_0 |\beta^{\text{modified}}(\omega, L)|^2 \, \mathrm{d}\omega \tag{35}$$

where $\beta^{\text{modified}}(\omega, L)$ is the absolute tip velocity FRF that can be obtained by modifying the relative tip displacement-to-base FRF, $\beta(\omega, L)$, [10, 24]:

$$\beta^{\text{modified}}(\omega, L) = \frac{1}{\mathrm{j}\omega} + \mathrm{j}\omega\beta(\omega, L). \tag{36}$$

Due to the first term in equation (36), the velocity FRF tends to infinity around 0 Hz as a singularity. Therefore a small frequency range of $[-\varepsilon, \varepsilon]$ is excluded in the integration of equation (35) to give

$$E[\dot{w}^2(L,t)] = \int_{-\bar{\omega}}^{-\varepsilon} S_0 |\beta^{\text{modified}}(\omega, L)|^2 \, \mathrm{d}\omega + \int_{\varepsilon}^{\bar{\omega}} S_0 |\beta^{\text{modified}}(\omega, L)|^2 \, \mathrm{d}\omega \tag{37}$$

where $\varepsilon \ll \omega_1$. Physically, this is well justified in the experiments since the shaker (excitation source) does not emulate motion at zero frequency (rigid body motion) and the neighborhood of 0 Hz is indeed excluded in the excitation signal. Using equation (20) in (36) yields single-mode solution for the modified absolute tip velocity FRF, and substituting the latter into equation (37) yields the single-mode solution for the mean-square tip velocity response.

4. Broadband random excitation: numerical solutions

4.1. Fourier series-based Runge–Kutta solution

The first numerical solution approach treats the given time series of the excitation in a deterministic fashion through its Fourier series representation. The excitation is then combined with the first-order equations for the numerical solution of the electroelastic response in the time domain.

The electroelastic state variables for the rth vibration mode are extracted from equations (6) and (7) as [38]

$$u_r^{(1)} = \eta_r(t), \qquad u_r^{(2)} = \dot{\eta}_r(t), \qquad u^{(3)} = v(t) \tag{38}$$

where $u_r^{(1)}$ is the modal displacement, $u_r^{(2)}$ is the modal velocity, and $u^{(3)}$ is the voltage output. Then the governing differential equations in the modal coordinates are expressed in the first-order form using $2M + 1$ equations as

$$\begin{bmatrix} \dot{u}_1^{(1)} & \dot{u}_2^{(1)} & \cdots & \dot{u}_M^{(1)} & \dot{u}_1^{(2)} & \dot{u}_2^{(2)} & \cdots & \dot{u}_M^{(2)} & \dot{u}^{(3)} \end{bmatrix}^t = \begin{bmatrix} u_1^{(2)} \\ u_2^{(2)} \\ \vdots \\ u_M^{(2)} \\ -2\zeta_1\omega_1 u_1^{(2)} - \omega_1^2 u_1^{(1)} + \tilde{\theta}_1 u^{(3)} + \sigma_1 a(t) \\ -2\zeta_2\omega_2 u_2^{(2)} - \omega_2^2 u_2^{(1)} + \tilde{\theta}_2 u^{(3)} + \sigma_2 a(t) \\ \vdots \\ -2\zeta_M\omega_M u_M^{(2)} - \omega_M^2 u_M^{(1)} + \tilde{\theta}_M u^{(3)} + \sigma_M a(t) \\ -u^{(3)}/R_\mathrm{l} C_\mathrm{p}^{\mathrm{eq}} - \tilde{\theta}_1 u_1^{(2)}/C_\mathrm{p}^{\mathrm{eq}} - \tilde{\theta}_2 u_2^{(2)}/C_\mathrm{p}^{\mathrm{eq}} - \cdots - \tilde{\theta}_M u_M^{(2)}/C_\mathrm{p}^{\mathrm{eq}} \end{bmatrix} \tag{39}$$

where $a(t)$ is the random base acceleration in the transverse direction ($a(t) = \ddot{g}(t)$), superscript t stands for the transpose and the solution is truncated after M modes. Note that three initial conditions are required for the state variables in mode r (we assume zero initial conditions in the simulations of this paper).

The random base acceleration history is represented as a deterministic input by using its Fourier series representation:

$$a(t) \cong p_0 + \sum_{k=1}^{N} \left[p_k \cos\left(k\frac{2\pi t}{T}\right) + q_k \sin\left(k\frac{2\pi t}{T}\right) \right] \tag{40}$$

where T is the length of the time history of base acceleration, p_0 is its mean value, while p_k and q_k ($k = 1, 2, \ldots$ are positive integers) are the Fourier coefficients given by

$$\begin{aligned} p_0 &= \frac{1}{T}\int_0^T a(t)\,\mathrm{d}t, \\ p_k &= \frac{2}{T}\int_0^T a(t)\cos\left(k\frac{2\pi t}{T}\right)\mathrm{d}t, \\ q_k &= \frac{2}{T}\int_0^T a(t)\sin\left(k\frac{2\pi t}{T}\right)\mathrm{d}t. \end{aligned} \tag{41}$$

In the Fourier series representation, the number of terms N is half of the total data points in the base acceleration history and p_0 is negligible for time typical acceleration data of ambient vibrations (hence zero mean value is assumed hereafter: $p_0 = 0$). Note that the foregoing representation and the resulting solution are strictly valid for the time interval of $[0, T]$ only. Equation (39) is then treated as a set of ordinary differential equations (ODEs). The computation is carried out by using an ODE solver, such as the ode45 algorithm in MATLAB, which uses an explicit Runge–Kutta formulation.

The time histories of the voltage output and modal velocities are obtained from the system of electroelastic ODEs. If the acceleration history has zero mean value, it is known that the response forms also have zero mean value. Thus the expected value of power output can be computed by using

$$E[P(t)] = \frac{1}{T}\int_0^T \frac{v^2(t)}{R_\mathrm{l}}\,\mathrm{d}t = \frac{\sigma_v^2}{R_\mathrm{l}} \tag{42}$$

where σ_v is the standard deviation of the voltage response.

Having obtained the modal coordinates, the tip velocity relative to moving base can be computed using

$$\dot{w}_{\text{rel}}(x,t) \cong \sum_{r=1}^{M} \phi_r(x)\dot{\eta}_r(t) = \phi_1(x)\dot{\eta}_1(t) + \phi_2(x)\dot{\eta}_2(t) + \cdots + \phi_M(x)\dot{\eta}_M(t). \tag{43}$$

Once again, comparison with the experimental results requires obtaining the absolute tip velocity response (relative to the fixed reference frame). Therefore, the velocity of the moving base is first computed from the base acceleration history by analytically integrating equation (40) and assuming $p_0 = 0$ (zero mean value for the base acceleration):

$$\dot{w}_{\text{base}}(t) \cong \sum_{k=1}^{N} \left[\frac{p_k T}{2\pi k} \sin\left(k\frac{2\pi t}{T}\right) - \frac{q_k T}{2\pi k} \cos\left(k\frac{2\pi t}{T}\right) \right]. \tag{44}$$

Superposing the time history of the base velocity to the relative tip velocity, the absolute tip velocity is obtained and its mean-square value can be calculated using

$$E[\dot{w}^2(L,t)] = \frac{1}{T}\int_0^T \dot{w}^2(L,t)\,\mathrm{d}t = \sigma_{\dot{w}}^2 \tag{45}$$

where $\sigma_{\dot{w}}$ is the standard deviation of the absolute tip velocity of the cantilever.

4.2. Euler–Maruyama solution

An alternative approach for the solution of equation (39) is to treat the problem as a set of stochastic differential equations (SDEs) and to use the Euler–Maruyama method [42] as done by Ferrari *et al* [27] and Litak *et al* [15], among others, for the SDOF problem, which is extended to cover multiple vibration modes here.

The voltage output and modal velocities are approximated by using the Euler–Maruyama scheme [42]:

$$\left[du_1^{(1)}\ du_2^{(1)}\ \cdots\ du_M^{(1)}\ du_1^{(2)}\ du_2^{(2)}\ \cdots\ du_M^{(2)}\ du^{(3)}\right]^t = \begin{bmatrix} u_1^{(2)} \\ u_2^{(2)} \\ \vdots \\ u_M^{(2)} \\ -2\zeta_1\omega_1 u_1^{(2)} - \omega_1^2 u_1^{(1)} + \tilde{\theta}_1 u^{(3)} \\ -2\zeta_2\omega_2 u_2^{(2)} - \omega_2^2 u_2^{(1)} + \tilde{\theta}_2 u^{(3)} \\ \vdots \\ -2\zeta_M\omega_M u_M^{(2)} - \omega_M^2 u_M^{(1)} + \tilde{\theta}_M u^{(3)} \\ -u^{(3)}/R_1 C_{\text{p}}^{\text{eq}} - \tilde{\theta}_1 u_1^{(2)}/C_{\text{p}}^{\text{eq}} - \tilde{\theta}_2 u_2^{(2)}/C_{\text{p}}^{\text{eq}} - \cdots - \tilde{\theta}_M u_M^{(2)}/C_{\text{p}}^{\text{eq}} \end{bmatrix} \mathrm{d}t + \left[0\ 0\ \cdots\ 0\ \sigma_1\ \sigma_2\ \cdots\ \sigma_M\ 0\right]^T \mathrm{d}W \tag{46}$$

where $\mathrm{d}W$ is the increment of Wiener process and is approximated as

$$\mathrm{d}W = a(t)\,\mathrm{d}t. \tag{47}$$

Since the Euler–Maruyama method requires a very fine time increment, the original time history of excitation input $a(t)$ is interpolated using a much higher sampling frequency of about 1 MHz (as compared to the original sampling frequency of 2560 Hz in the following experiments). The interpolated acceleration history is then checked to ensure that its standard deviation and mean remain the same as the original history. Following the Euler–Maruyama scheme, after obtaining the time histories of voltage and modal coordinates, the expected value of power output can be computed using equation (42), and the time history of tip velocity relative to the moving base can be computed using equation (43). In order to obtain the absolute tip velocity (relative to the fixed reference frame), we again use the Fourier series representation of the velocity of the base, as done in the previous section. The base velocity is also interpolated (and checked for its mean and standard deviation) and then superimposed on the relative tip velocity, and the mean-square value of the absolute tip velocity is calculated using equation (45).

5. Experimental validations

5.1. Experimental setup and bimorph cantilever

A brass-reinforced PZT-5H piezoelectric bimorph (T226-H4-103X by Piezo Systems Inc.) is employed for the model validation experiments. In the experimental setup (figure 2), the bimorph is clamped at one end (shaker side) and free at the other end. The bimorph cantilever (figure 3(a)) is composed of two PZT-5H layers (with thin nickel electrodes covering the transverse faces) bracketing a brass layer, as shown in the close-up side view photo of figure 3(b), and its basic properties are listed in table 2. The brass layer provides the electrical conductivity between the inner electrodes of the oppositely poled PZT-5H layers, and therefore the configuration employs the series connection of the piezoelectric layers (figure 1(a)). An accelerometer is attached on the top surface of the aluminum clamp and the clamp is attached onto the armature of an electromechanical shaker. Since the clamp is assumed to behave like a rigid body in the frequency range of interest, the accelerometer measures the base acceleration, $a(t)$. A laser vibrometer measures the tip velocity in the lateral (vertical) direction. A resistor box is connected to the electrode terminals of the bimorph and the voltage across the electrical load is measured for several resistance values ranging from the short-circuit to open-circuit conditions. Three input channels of the data acquisition system are used. The first channel (the reference channel) records the acceleration processed by a signal conditioner, the second channel records the voltage measured across the resistive load, and the third channel measures the tip velocity measured by the laser vibrometer.

5.2. Experimental and analytical electroelastic FRFs

Prior to the broadband random vibration experiments, low-amplitude chirp excitation tests are conducted for the purpose of obtaining the linear electroelastic response FRFs of the system. Figure 4 shows that the analytical voltage and tip velocity FRFs are in very good agreement with

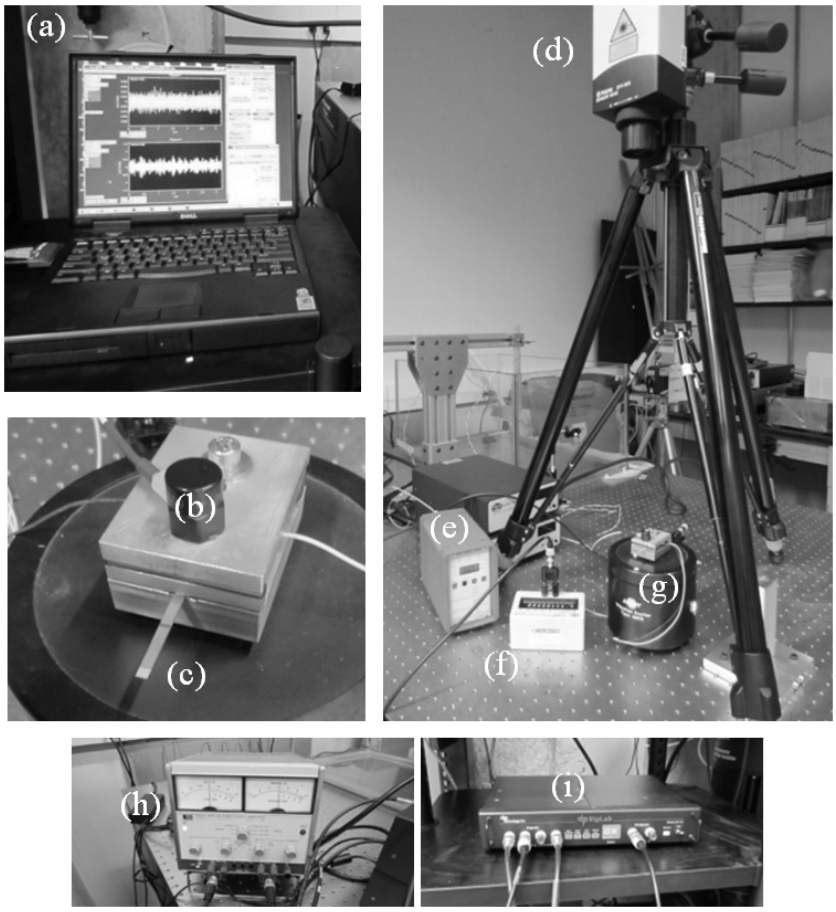

Figure 2. Details of the experimental setup: (a) computer with data acquisition software; (b) accelerometer on the clamp mounted to the armature of the shaker; (c) piezoelectric bimorph cantilever; (d) laser vibrometer; (e) signal conditioner; (f) resistor box; (g) shaker; (h) power supply/amplifier; and (i) data acquisition hardware.

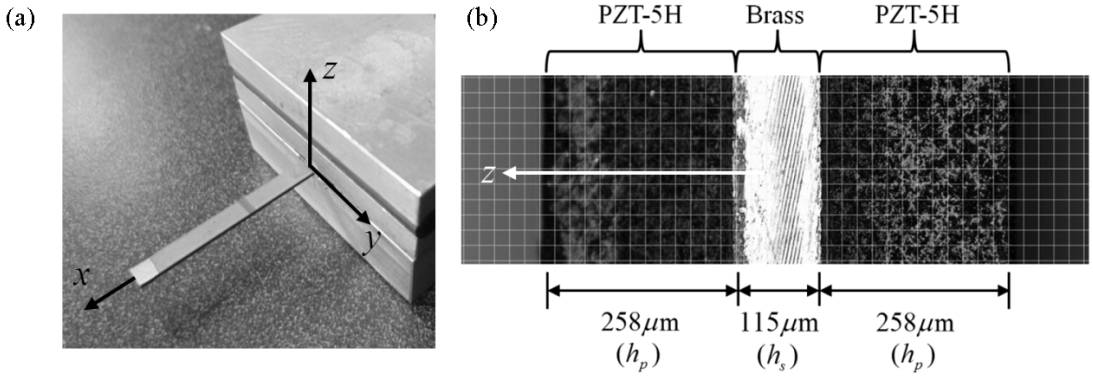

Figure 3. (a) Close-up view of the brass-reinforced bimorph cantilever shown in figure 2(c) and (b) its side view displaying the thicknesses of piezoelectric and substructure layers. The brass layer provides the electrical conductivity between the inner electrodes of the oppositely poled piezoelectric layers.

the experimental results for a set of resistors ranging from short-circuit to open-circuit conditions. Note that the base acceleration in these FRFs is given in terms of the gravitational acceleration, $g = 9.81$ m s^{-2}. Close-up views around the fundamental vibration mode are also displayed in these figures, verifying the accuracy of the distributed-parameter model in predicting the shift in the fundamental resonance frequency with changing load resistance. Recall that the analytical multi-mode FRFs are due to equations (13) and (36) for the voltage and the absolute velocity response, respectively. The modal mechanical damping ratios of the first and the second modes covered in the experimental measurements are obtained as 0.64% and 0.75%, respectively, i.e., $\zeta_1 = 0.0064$ and $\zeta_2 = 0.0075$. It is important to note

Table 2. Geometric and material properties of the PZT-5H bimorph cantilever used in experiments.

	Piezoceramic (PZT-5H)	Substructure (brass)
Length (mm)	27	27
Width (mm)	3.2	3.2
Thickness (mm)	0.258 (each)	0.115
Mass density (kg m^{-3})	7500	9000
Elastic modulus (GPa)	60.6	105
Piezoelectric constant (C m^{-2})	−16.6	—
Permittivity constant (nF m^{-1})	25.55	—

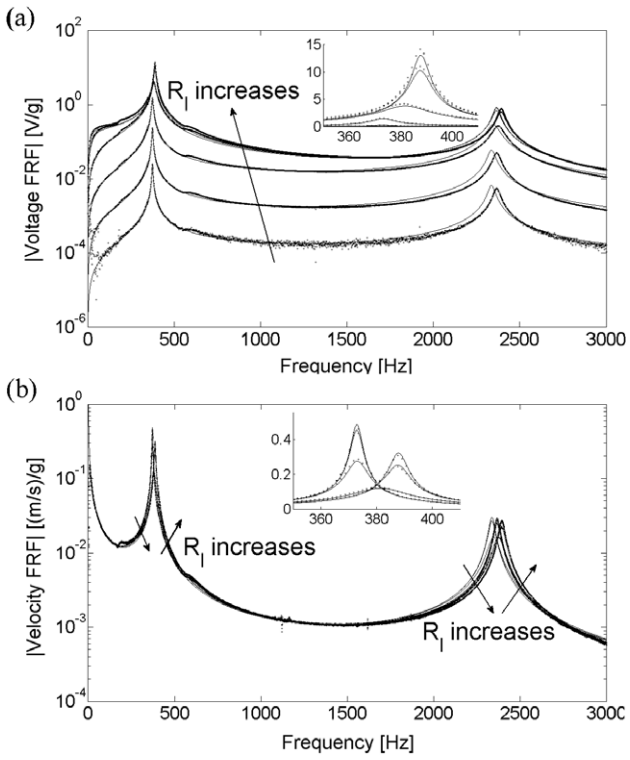

Figure 4. Experimental validation of the electroelastic FRFs: (a) voltage and (b) tip velocity FRFs of the PZT-5H bimorph for a set of resistors (100Ω, 1 kΩ, 10 kΩ, 91 kΩ, 500 kΩ, and 910 kΩ). Solid lines are the analytical predictions and dots are the experimental measurements.

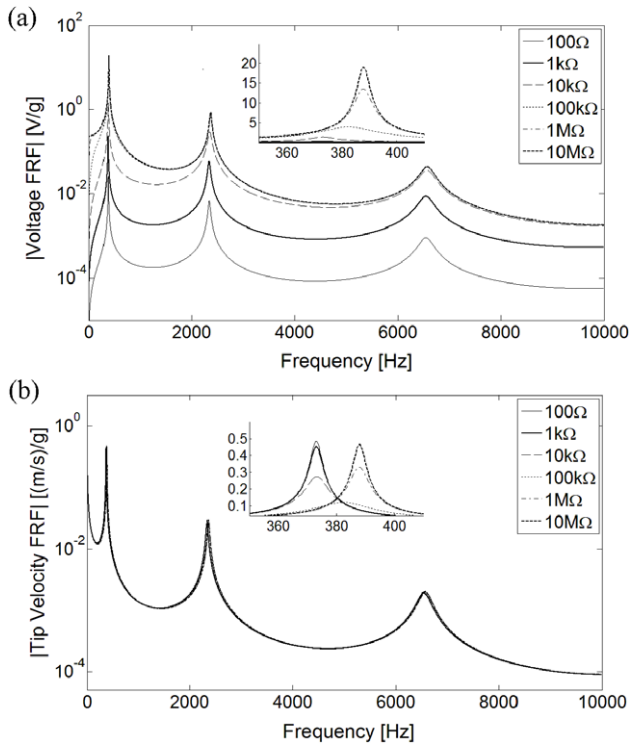

Figure 5. Analytically obtained (a) voltage and (b) tip velocity FRFs of the PZT-5H bimorph for a set of resistors in the frequency range of 0–10 kHz.

that these are the purely mechanical damping ratios in the absence of electrical (shunt) damping. Typically, it is convenient to identify these damping ratios in short-circuit or open-circuit conditions if conventional methods (half-power points, logarithmic decrement, etc) [40] are to be used instead of electromechanical identification expressions in the presence of finite shunt resistance [19].

The extension of the analytical FRF simulations to cover the frequency range of 0–10 kHz (hence the first three vibration modes) is shown in figure 5, where the damping ratios for mode 3 as well as higher modes which are outside the range of 0–10 kHz are calculated by using the identified damping ratios of the first two modes in the proportional (Rayleigh) damping equations [38, 43]. Having validated the electroelastic FRFs of the system, broadband random excitation experiments are conducted next.

5.3. Broadband random excitation

In the random excitation experiments, the base excitation is intended to cover a broad range of excitation frequencies to be as close to white noise as possible within the limitations of the electromechanical shaker and other hardware. A sample of time history of acceleration in a broadband random excitation test is shown in figure 6 along with its PSD. Several experiments (not discussed here) show that the PSD of base acceleration is fairly flat up to 3 kHz (which covers the first two vibration modes of the harvester) and gradually decays above this value due to device (mainly shaker) limitations, although the software used in signal generation is theoretically capable of feeding signal input up to 20 kHz.

A resistor sweep from 500 Ω (close to short-circuit condition) to 1 MΩ (close to open-circuit condition) is performed. Note that these resistance values are, respectively, close to short- and open-circuit conditions for the specific

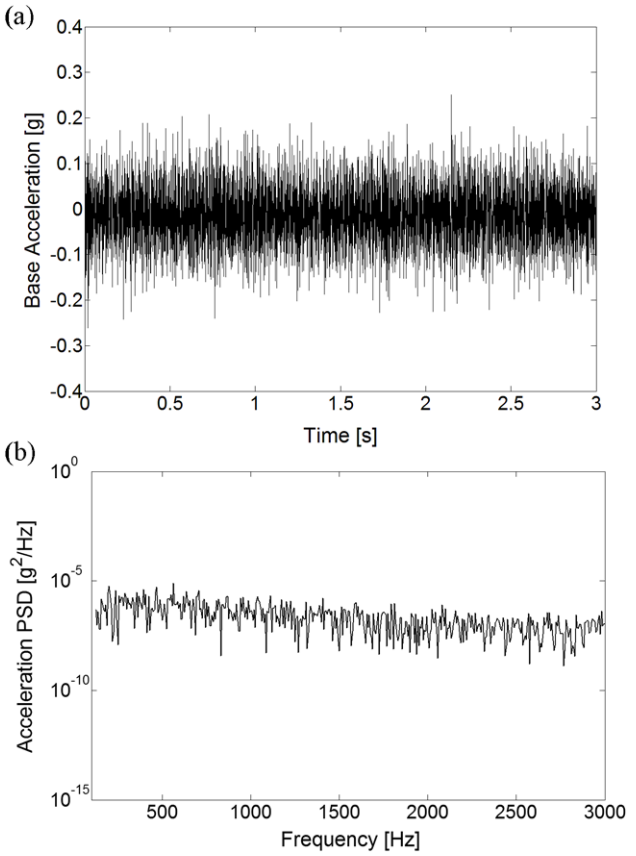

Figure 6. (a) A sample of time history of the measured random base acceleration (approximate PSD:1.7 mg^2 Hz^{-1}) and (b) its PSD for a broad frequency range.

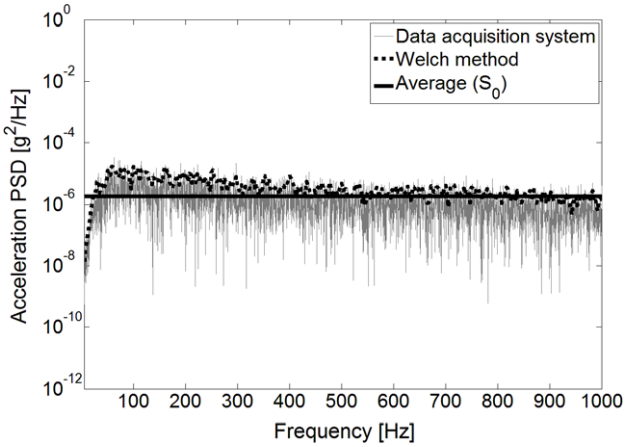

Figure 7. PSD of base acceleration shown in figure 6 extracted directly from the data acquisition system, estimated using the Welch method, and averaged based on the Welch estimate.

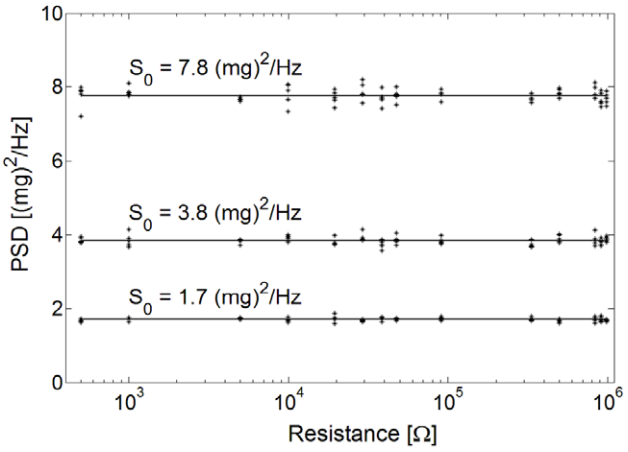

Figure 8. PSD values estimated from the Welch algorithm for all tests at three base excitation levels (1.7, 3.8, and 7.8 mg^2 Hz^{-1}) along with the average PSD values at each level (a total of 210 different time series).

bimorph cantilever and the range of excitation frequencies studied here. In each set of experiments, base acceleration, voltage output, and tip velocity are recorded for 3.2 s. For each resistive load, the test is repeated five times. From equations (42) and (45), the expected (mean) power and mean-square tip velocity are computed. The same experimental procedure is repeated for three different excitation levels sent to the shaker. While the data acquisition system (SigLab) extracts the PSD of base acceleration, we also estimate this PSD from the time history using the Welch method in MATLAB, which is a commonly used algorithm in PSD estimation. A sampling frequency of 2560 Hz is used in the estimation. Shown in figure 7 are the experimentally extracted PSD (from the data acquisition system), the estimated PSD based on the Welch method, and the averaged PSD for the base acceleration history shown in figure 6.

In the analytical solution, the base excitation is assumed to be ideal Gaussian white noise with a constant PSD, S_0. In order to obtain the constant value of S_0, the relatively flat portion of the Welch estimate is used and an average value is extracted. For instance, using the Welch estimate shown in figure 7, we identify $S_0 = 1.7$ mg^2 Hz^{-1} for the base acceleration history given in figure 6. This estimation is performed for the time history of base acceleration in each of the tests and the mean values are obtained. As shown in figure 8 for 70 different time series for each PSD level (14 different resistors and 5 time series at each level), it can be concluded that the shaker generates excitations with good consistency in the base acceleration PSD. Therefore, it is reasonable to use the mean PSD in the analytical solution for all resistance values, while the individual time histories are used in the ODE-based and SDE-based numerical solutions toward predicting the expected value of the electrical power and mean-square value of the shunted vibration response.

5.4. Expected value of the electrical power output

At each level of base excitation, the experimental measurements are plotted and compared against the analytical and numerical predictions. An example case is given in figure 9(a) for the excitation PSD level of 1.7 mg^2 Hz^{-1}. Very good agreement is observed between the experimental results and model predictions (both analytical and numerical). The difference between single-mode and multi-mode analytical solutions is due to the effect of higher vibration modes,

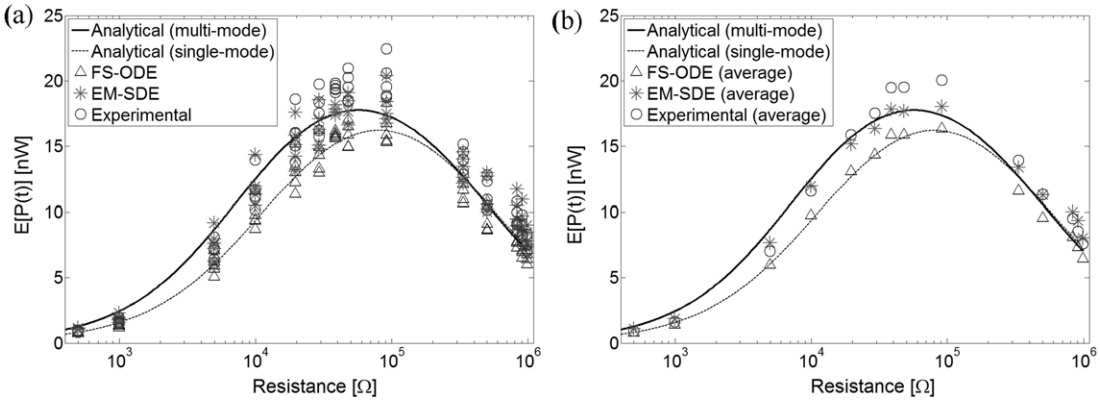

Figure 9. Comparison of the analytical and numerical simulations of mean power output with the experimental measurements for a set of resistive loads showing (a) five experimental and numerical data points at each resistor and (b) only average values for clarity (PSD level of base acceleration: 1.7 mg^2 Hz^{-1}). In the legends, the Fourier series-based ODE solution is denoted by FS-ODE while the SDE solution based on the Euler–Maruyama scheme is denoted by EM-SDE.

considering the lightly damped nature of the second vibration mode (see figure 4). Both numerical solutions employ only the first vibration mode to minimize the computational time, while the analytical solutions can easily include several vibration modes (10 modes are used in the simulations). The analytical solutions use the frequency-domain integration range of (−10 kHz, 10 kHz), i.e., $\bar{\omega} = 10$ kHz in section 3. It is also important to note that, in the analytical predictions, an average value of PSD is used for all resistors. However, in each of the numerical simulations, the respective time history of base acceleration is directly employed as the input. Consequently, at each value of electrical resistance, the Fourier series-based ODE solution and the SDE solution based on the Euler–Maruyama method (as well as the experimental measurements) have five different data points in figure 9(a). Note that one can easily take the averages of the experimental and numerical data points of five separate random data series at each resistor to simplify figures 9(a) and (b) for clarity.

The analytical predictions, numerical simulations, and experimental measurements for three levels of base acceleration PSD are plotted in figure 10(a) (and the version based on averaging the numerical and experimental data points at each resistor is shown in figure 10(b)). The base excitation levels are represented in terms of their averaged PSD values following figure 8. Both the analytical and numerical predictions of the expected power exhibit very good agreement with the experimental results. The multi-mode analytical solution more accurately predicts the experimental results around the optimal resistance region at each PSD level. It should be noted that the horizontal axis is on a logarithmic scale and the optimal electrical load in the single-mode and multi-mode analytical predictions are substantially different although the amplitude-wise difference is relatively small.

5.5. Mean-square value of the shunted vibration response

The single-mode and multi-mode analytical, numerical, and experimental results of the tip velocity at excitation level of 1.7 mg^2 Hz^{-1} are compared in figure 11. As in the case of power generation, the analytical and numerical simulations of the tip velocity response match very well with experimental results. The mean-square of vibration response is observed to be relatively insensitive to the higher-mode effects. Comparisons across different excitation levels are summarized in figure 12, with very good predictions particularly around the optimal loads of the maximum power output and minimum vibration response.

The maximum expected power output and the minimum mean-square tip velocity response versus input PSD are plotted in figures 13(a) and (b), respectively. We recall that the analytical solutions for the expected power and mean-square tip velocity are due to equations (21) and (35), respectively, where the proportionality of the left hand side (mean power or mean-square tip velocity) to the input PSD is evident for the case of white noise excitation, since the S_0 term can be taken outside the integral.

6. Conclusions

Analytical and numerical solutions, and experimental validations of piezoelectric energy harvesting from broadband random vibrations are presented based on a distributed-parameter electroelastic model. The analytical solution uses the combination of distributed-parameter electroelastic FRFs with the input power spectral density (PSD) while the numerical solutions treat the random base excitation problem in two separate approaches, deterministically and stochastically. The deterministic approach represents the base acceleration history in terms of its Fourier series expansion to use with the first-order electroelastic equations in an ordinary differential equation (ODE) solver, while the stochastic approach directly employs an Euler–Maruyama scheme to solve the resulting first-order stochastic differential equations (SDEs). The expected (mean) piezoelectric power output and the mean-square vibration response forms are investigated for a broad range of resistive loads spanning from the short-circuit to open-circuit conditions. The shunt damping

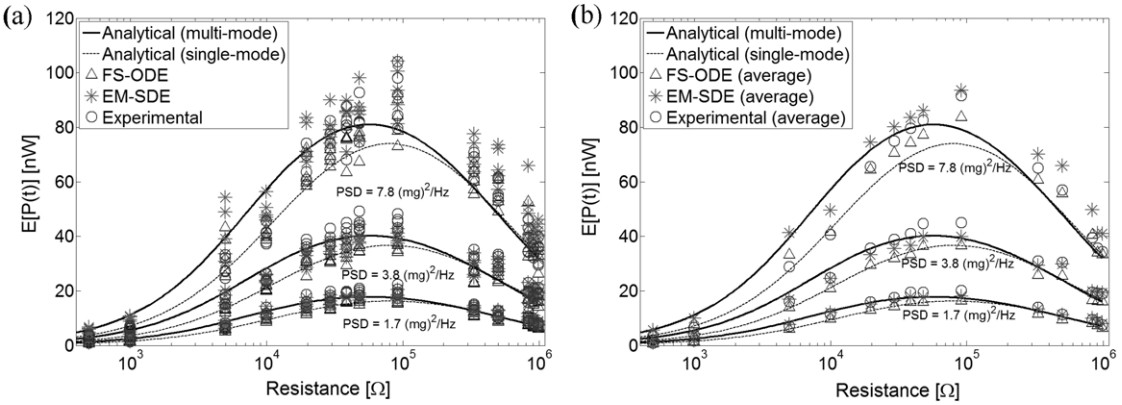

Figure 10. Comparison of the analytical and numerical simulations of mean power output with the experimental measurements for a set of resistive loads at different PSD levels of base acceleration (1.7, 3.8, and 7.8 mg^2 Hz^{-1}) showing (a) five experimental and numerical data points at each resistor and (b) only average values for clarity. In the legends, the Fourier series-based ODE solution is denoted by FS-ODE while the SDE solution based on the Euler–Maruyama scheme is denoted by EM-SDE.

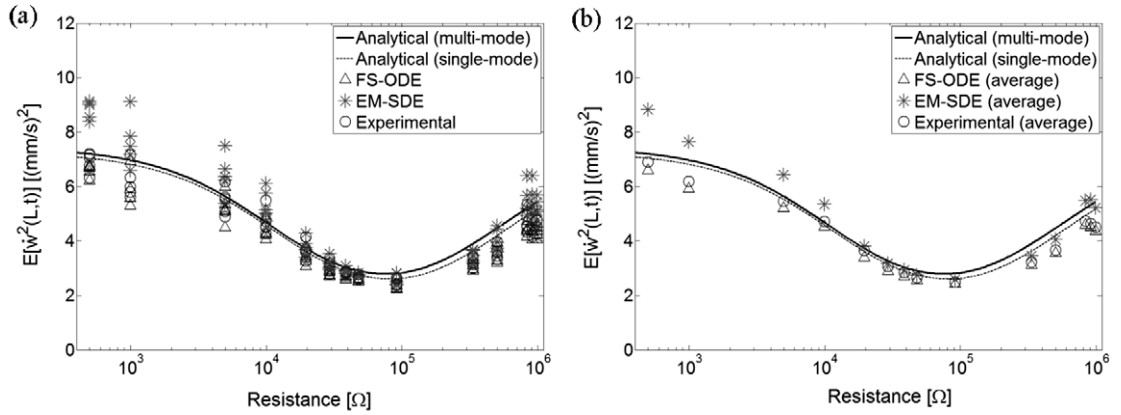

Figure 11. Comparison of the analytical and numerical simulations of mean-square shunted tip velocity with the experimental measurements for a set of resistive loads showing (a) five experimental and numerical data points at each resistor and (b) only average values for clarity (PSD level of base acceleration:1.7 mg^2 Hz^{-1}). In the legends, the Fourier series-based ODE solution is denoted by FS-ODE while the SDE solution based on the Euler–Maruyama scheme is denoted by EM-SDE.

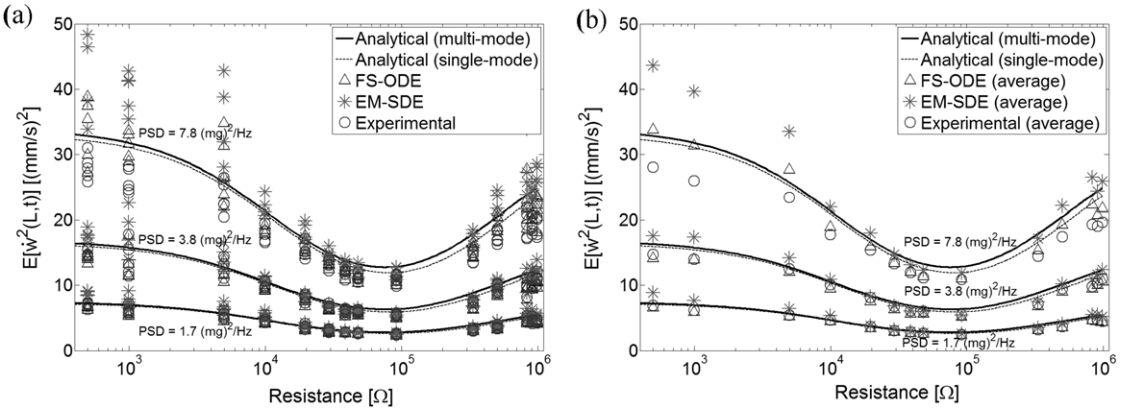

Figure 12. Comparison of the analytical and numerical simulations of mean-square shunted tip velocity with the experimental measurements for a set of resistive loads at different PSD levels of base acceleration (1.7, 3.8, and 7.8 mg^2 Hz^{-1}) showing (a) five experimental and numerical data points at each resistor and (b) only average values for clarity. In the legends, the Fourier series-based ODE solution is denoted by FS-ODE while the SDE solution based on the Euler–Maruyama scheme is denoted by EM-SDE.

effect associated with random piezoelectric power generation is also reported. The analytical, as well as ODE-based and SDE-based numerical predictions exhibit very good agreement with the experimental measurements taken for a brass-reinforced PZT-5H piezoelectric energy harvester. The analytical and numerical solutions are further validated for different PSD levels of random excitation. It is observed that the expected power and mean-square vibration response

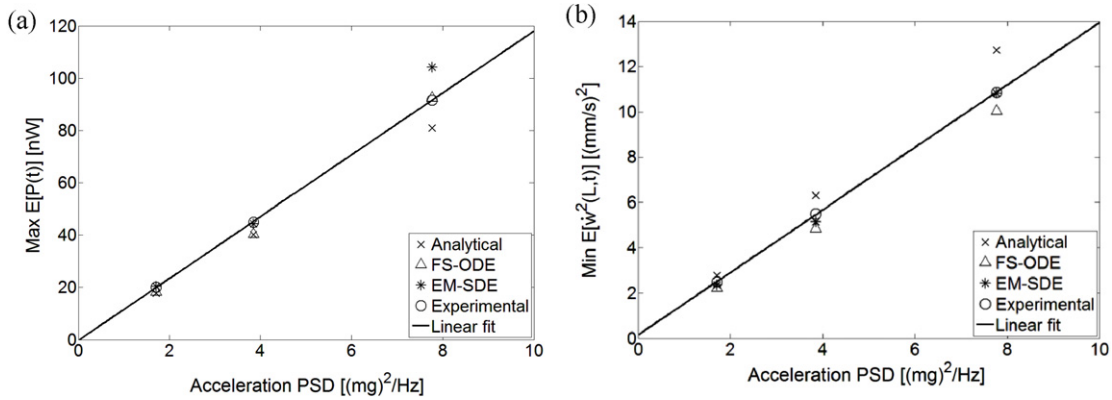

Figure 13. (a) Maximum expected power output and (b) minimum mean-square shunted tip velocity at different levels of base acceleration PSD exhibiting linear dependence between the maximum expected power, minimum mean-square tip velocity, and base acceleration PSD.

depend on the input (base acceleration) PSD linearly. Based on the analytical solution, the effect of higher vibration modes is also investigated and it is concluded that lightly damped higher modes can alter the expected power curve (primarily the optimal load) if the PSD of input vibration covers high frequencies as in the case of white noise excitation.

Acknowledgments

Support from the US Department of Commerce, National Institute of Standards and Technology, Technology Innovation Program, Cooperative Agreement Number 70NANB9H9007, 'Self-Powered Wireless Sensor Network for Structural Health Prognosis', is gratefully acknowledged.

References

[1] Beeby S P, Tudor M J and White N M 2006 Energy harvesting vibration sources for microsystems applications *Meas. Sci. Technol.* **17** R175–95
[2] Priya S 2007 Advances in energy harvesting using low profile piezoelectric transducers *J. Electroceram.* **19** 167–84
[3] Anton S R and Sodano H A 2007 A review of power harvesting using piezoelectric materials (2003–2006) *Smart Mater. Struct.* **16** R1–R21
[4] Cook-Chennault K A, Thambi N and Sastry A M 2008 Powering MEMS portable devices—a review of non-regenerative and regenerative power supply systems with special emphasis on piezoelectric energy harvesting systems *Smart Mater. Struct.* **17** 043001
[5] Hudak N S and Amatucci G G 2008 Small-scale energy harvesting through thermoelectric, vibration, and radiofrequency power conversion *J. Appl. Phys.* **103** 101301
[6] Amirtharajah R and Chandrakasan A P 1998 Self-powered signal processing using vibration-based power generation *IEEE J. Solid-State Circuits* **33** 687–95
[7] Roundy S, Wright P K and Rabaey J 2003 A study of low level vibrations as a power source for wireless sensor nodes *Comput. Commun.* **26** 1131–44
[8] Mitcheson P D *et al* 2004 MEMS electrostatic micropower generator for low frequency operation *Sensors Actuators* A **115** 523–9
[9] duToit N E, Wardle B L and Kim S G 2005 Design considerations for MEMS-scale piezoelectric mechanical vibration energy harvesters *Integr. Ferroelectr.* **71** 121–60
[10] Wang L and Yuan F G 2008 Vibration energy harvesting by magnetostrictive material *Smart Mater. Struct.* **17** 045009
[11] Erturk A and Inman D J 2009 An experimentally validated bimorph cantilever model for piezoelectric energy harvesting from base excitations *Smart Mater. Struct.* **18** 025009
[12] Mann B P and Sims N D 2009 Energy harvesting from the nonlinear oscillations of magnetic levitation *J. Sound Vib.* **319** 515–30
[13] Stanton S C *et al* 2010 Nonlinear piezoelectricity in electroelastic energy harvesters: modeling and experimental identification *J. Appl. Phys.* **108** 074903
[14] Friswell M I and Adhikari S 2010 Sensor shape design for piezoelectric cantilever beams to harvest vibration energy *J. Appl. Phys.* **108** 014901
[15] Bai X L *et al* 2012 A magnetoelectric energy harvester with the magnetic coupling to enhance the output performance *J. Appl. Phys.* **111** 07A938
[16] Aureli M *et al* 2010 Energy harvesting from base excitation of ionic polymer metal composites in fluid environments *Smart Mater. Struct.* **19** 015003
[17] Shu Y C and Lien I C 2006 Analysis of power output for piezoelectric energy harvesting systems *Smart Mater. Struct.* **15** 1499–512
[18] Renno J M, Daqaq M F and Inman D J 2009 On the optimal energy harvesting from a vibration source *J. Sound Vib.* **320** 386–405
[19] Erturk A and Inman D J 2011 Parameter identification and optimization in piezoelectric energy harvesting: analytical relations, asymptotic analyses, and experimental validations *Proc. Inst. Mech. Eng.* I *J. Syst. Control Eng.* **225** 485–96
[20] Stanton S C, Owens B A M and Mann B P 2012 Harmonic balance analysis of the bistable piezoelectric inertial generator *J. Sound Vib.* **331** 3617–27
[21] Halvorsen E 2008 Energy harvesters driven by broadband random vibrations *J. Microelectromech. Syst.* **17** 1061–71
[22] Adhikari S, Friswell M I and Inman D J 2009 Piezoelectric energy harvesting from broadband random vibrations *Smart Mater. Struct.* **18** 115005
[23] Scruggs J T 2009 An optimal stochastic control theory for distributed energy harvesting networks *J. Sound Vib.* **320** 707–25
[24] Daqaq M F 2010 Response of uni-modal duffing-type harvesters to random forced excitations *J. Sound Vib.* **329** 3621–31
[25] Barton D A W, Burrow S G and Clare L R 2010 Energy harvesting from vibrations with a nonlinear oscillator *J. Vib. Acoust.-Trans. ASME J. Vib. Acoust.* **132** 021009

[26] Gammaitoni L, Neri I and Vocca H 2009 Nonlinear oscillators for vibration energy harvesting *Appl. Phys. Lett.* **94** 164102
[27] Ferrari M *et al* 2009 Improved energy harvesting from wideband vibrations by nonlinear piezoelectric converters *Proc. Eurosensors Xxiii Conf.* **1** 1203–6
[28] Litak G, Friswell M I and Adhikari S 2010 Magnetopiezoelastic energy harvesting driven by random excitations *Appl. Phys. Lett.* **96** 214103
[29] Erturk A, Hoffmann J and Inman D J 2009 A piezomagnetoelastic structure for broadband vibration energy harvesting *Appl. Phys. Lett.* **94** 254102
[30] McInnes C R, Gorman D G and Cartmell M P 2008 Enhanced vibrational energy harvesting using nonlinear stochastic resonance *J. Sound Vib.* **318** 655–62
[31] Ali S F, Adhikari S and Friswell M I 2011 Analysis of magnetopiezoelastic energy harvesters under random excitations: an equivalent linearization approach *SPIE Smart Structures and Materials + Nondestructive Evaluation and Health Monitoring* **7977** 79770N
[32] Daqaq M F 2011 Transduction of a bistable inductive generator driven by white and exponentially correlated Gaussian noise *J. Sound Vib.* **330** 2554–64
[33] Nguyen D S *et al* 2010 Fabrication and characterization of a wideband MEMS energy harvester utilizing nonlinear springs *J. Micromech. Microeng.* **20** 125009
[34] Halvorsen E, Blystad L-C J, Husa S and Westby E 2007 Simulation of electromechanical systems driven by large random vibrations *MEMSTECH: Int. Conf. Perspective Technologies and Methods in MEMS Design* 117–22
[35] Tvedt L G W, Blystad L C J and Halvorsen E 2008 Simulation of an electrostatic energy harvester at large amplitude narrow and wide band vibrations *Dtip 2008: Symp. on Design, Test, Integration and Packaging of Mems/Moems* pp 296–301
[36] Blystad L C J, Halvorsen E and Husa S 2010 Piezoelectric MEMS energy harvesting systems driven by harmonic and random vibrations *IEEE Trans. Ultrason. Ferroelectr. Freq. Control* **57** 908–19
[37] Tvedt L G W, Nguyen D S and Halvorsen E 2010 Nonlinear behavior of an electrostatic energy harvester under wide- and narrowband excitation *J. Microelectromech. Syst.* **19** 305–16
[38] Erturk A and Inman D J 2011 *Piezoelectric Energy Harvesting* vol xx (Wiley: Chichester) p 392
[39] Erturk A 2012 Assumed-modes modeling of piezoelectric energy harvesters: Euler–Bernoulli, Rayleigh, and Timoshenko models with axial deformations *Computers and Structures* doi:10.1016/j.compstruc.2012.05.010
[40] Meirovitch L 2001 *Fundamentals of Vibrations* vol xviii (Boston: McGraw-Hill) p 806
[41] Newland D E 1975 *An Introduction to Random Vibrations and Spectral Analysis* vol xxi (London; New York: Longman) p 285
[42] Kloeden P E and Platen E 1992 Numerical solution of stochastic differential equations *Applications of Mathematics* vol xxxv (Berlin: Springer) p 632
[43] Clough R W and Penzien J 1993 *Dynamics of Structures* 2nd edn, vol xxii (New York: McGraw-Hill) p 738